Adjoint - based Aeroacoustics Design Optimization for Blade Vortex Interaction Noise

Enrico Fabiano [*]   Dimitri Mavriplis [†]

Jay Sitaraman [‡]

Department of Mechanical Engineering,University of Wyoming, Laramie, WY 82071-3295.

This paper presents the development and application of an adjoint-based optimization method to designing airfoils with the objective of mitigating airfoil - vortex interaction noise without incurring severe performance penalties. The unsteady flow problem is simulated with an in-house two dimensional Euler finite volume solver. The acoustic analysis is performed using a two-dimensional formulation of the FW-H equation in the frequency domain. The corresponding adjoint codes that compute the sensitivities of the optimization objective functions with respect to the design variables are developed through linearization of each component of the aerodynamic and acoustic solvers respectively. The newly developed adjoint formulation is then used to perform airfoil design optimization on a NACA 0012 airfoil while constraining the time-integrated lift coefficient to the baseline value. Results are presented for different optimization algorithms.

I.   Introduction

With the ever more stringent noise requirements that rotorcraft must meet, rotor acoustics takes on a leading role in the helicopter design process. Among the many sources of noise associated with the complex aerodynamics of rotors, blade vortex interaction (BVI), since it usually occours at certification flight condition, is of particular importance not only because it can adversely impact the rotors' performance, but also because it negatively affects the helicopter noise signature as it tends to propagate out of the plane of the rotor, towards the ground.[1]

For these reasons, in the recent past, blade vortex interaction has been the subject of numerous experimental and numerical investigations. As a consequence the fundamental mechanism underlying blade vortex interaction noise is now farily well understood. Numerous passive techniques have been implemented in an attempt to minimize BVI noise, but all of these techniques have had detrimental consequences on the aerodynamic performances of rotors.[2,3] The goal of this paper is to develop a CFD-based aeroacoustic optimization tool so that optimal passive noise minimization techniques can be exploited without incurring significant performance penalties. Through the application of optimal shape modifications, aerodynamic shape optimization is often used to meet unique performance requirements. The use of shape optimization for steady-state problems is now fairly well established in the aircraft industry, where two-dimensional airfoil optimization techniques have seen widespread use since their initial appearances decades ago.[4] Adjoint techniques have played a major role in gradient-based steady-state aerodynamic optimization, especially in 3D, since the full sensitivity vector of a single objective with respect to any number of design variables can be computed with a single adjoint solution, at a cost roughly equivalent to a single flow solution.[5–10]

On the contrary adjoint methods for unsteady problems have received less attention,[11–14] their development having been hindered by the inherent computational cost and the complexity of the associated flow physics. Recently unsteady adjoint techniques have been proposed for both two-dimensional[12,14–16] and three-dimensional[13,17] problems. Furthermore adjoint formulations for three-dimensional coupled problems, such as aeroelasticity, have been recently proposed.[18]

To evaluate the acoustic signature and its derivative at a farfield observer a hybrid approach has been developed: a near-field CFD solver provides the input to the acoustic module that propagates the acoustic pressure at the far-field observer location. The CFD solver used here is an in-house Euler two-dimensional finite-volume solver augmented

---

[*]Phd Candidate; efabiano@uwyo.edu

[†]Professor; mavripl@uwyo.edu

[‡]Assistant Professor; jsitaram@uwyo.edu

American Institute of Aeronautics and Astronautics

with steady and unsteady discrete adjoint capability. The acoustic propagation code is a two-dimensional formulation of the FW-H equation in the frequency domain[19] for which the adjoint formulation has been developed in this work. The paper is structured as follows: section II introduces the CFD solver used in this work, section III details the test problem chosen to validate the proposed methodolgy, section IV presents the adjoint linearization of the flow solver, section V details the acoustic module and its linearization, section VI presents the coupling between the aerodynamic and the acoustic codes and finally section VII explains the optimization results.

II. Aerodynamic Analysis

II.A. Flow Solver Analysis Formulation

The base flow solver used in this work is an in-house unstructured-mesh Euler solver that has been validated for steady-state and time-dependent flows and contains a discrete tangent and adjoint sensitivity capability for both steady state and time-dependent flow problems. The flow solver is based on the conservative form of the Euler equations which may be written as:

$$\frac{\partial \mathbf{V}\mathbf{U}(\mathbf{x},t)}{\partial t} + \nabla \cdot \mathbf{F}(\mathbf{U}) = 0 \tag{1}$$

where $\mathbf{V}$ refers to the area of the control volume, the state vector $\mathbf{U}$ consists of the conserved variables in the Euler equations and the flux vector $\mathbf{F} = \mathbf{F}(\mathbf{U})$ contains the inviscid flux. The equations are closed with the perfect gas equation of state.

The solver uses a cell-centered control volume formulation that is second-order accurate, where the inviscid flux integral S around a closed control volume is discretized as:

$$S = \int_{dB} [\mathbf{F}(\mathbf{U})] \cdot \mathbf{n}dB = \sum_{i=1}^{n_{edge}} \mathbf{F}_{e_i}^{\perp}(\mathbf{U}, \mathbf{n}_{ei})B_{e_i} \tag{2}$$

where B_e is the edge length, $\mathbf{n}_e$ is the unit normal of the edge, and $F_e^{\perp}$ is the normal flux across the edge. The normal flux across the edge is computed using the second-order accurate matrix dissipation scheme[20] as the sum of a central difference and an artificial dissipation term as shown below,

$$\begin{aligned}
\mathbf{F}_e^{\perp} &= \frac{1}{2}\left\{ \mathbf{F}_L^{\perp}(\mathbf{U}_L, V_e, \mathbf{n}_e) + \mathbf{F}_R^{\perp}(\mathbf{U}_R, V_e, \mathbf{n}_e) \right. \\
&\left. + \kappa^{(4)}[T]|[\lambda]|[T]^{-1}\left\{ (\nabla^2\mathbf{U})_L - (\nabla^2\mathbf{U})_R \right\} \right\}
\end{aligned} \tag{3}$$

where $\mathbf{U}_L$, $\mathbf{U}_R$ are the left and right state vectors and $(\nabla^2\mathbf{U})_L$, $(\nabla^2\mathbf{U})_R$ are the left and right undivided Laplacians computed for any element i as

$$(\nabla^2\mathbf{U})_i = \sum_{k=1}^{neighbors} (\mathbf{U}_k - \mathbf{U}_i) \tag{4}$$

The time derivative term is discretized using a second-order accurate backward-difference formula (BDF2) scheme as:

$$\frac{\partial V\mathbf{U}}{\partial t} = \frac{\frac{3}{2}V\mathbf{U}^n - 2V\mathbf{U}^{n-1} + \frac{1}{2}V\mathbf{U}^{n-2}}{\Delta t} \tag{5}$$

The index n is used to indicate the current time-level as the convention throughout the paper. The discretization of the BDF2 scheme shown in equation (5) is based on a uniform time-step size.

Denoting the spatial residual at time level n by the operator $S^n(\mathbf{U}^n)$, the resulting system of non-linear equations to be solved for the analysis problem at each time step can be written as:

$$\mathbf{R}^n = \mathbf{R}^n(\mathbf{U}^n, \mathbf{U}^{n-1}, \mathbf{U}^{n-2}) = \frac{\frac{3}{2}V\mathbf{U}^n - 2V\mathbf{U}^{n-1} - \frac{1}{2}V\mathbf{U}^{n-2}}{\Delta t} + \mathbf{S^n}(\mathbf{U^n}) = \mathbf{0} \tag{6}$$

At each time step n, the implicit residual is linearized with respect to the unknown solution vector $\mathbf{U}^n$ and solved for using Newton's method as:

$$\left[\frac{\partial \mathbf{R}^k}{\partial \mathbf{U}^k}\right]\delta\mathbf{U}^k = -\mathbf{R}^k \tag{7}$$

$$\mathbf{U}^{k+1} = \mathbf{U}^k + \delta\mathbf{U}^k$$

$$\delta\mathbf{U}^k \to 0, \mathbf{U}^n = \mathbf{U}^k$$

American Institute of Aeronautics and Astronautics

The Jacobian matrix is inverted iteratively using a GMRES Krylov solver preconditioned with a coloured Gauss-Seidel algorithm.

II.B. Mesh deformation capability

In order to deform the mesh for optimization purposes, a spring analogy approach has been implemented. In this approach the mesh is seen as a network of interconnected springs whose coefficients are assumed to be inversely proportional to the second power of the edges length. Two independent force balance equations are formulated for each node in response to the surface displacements. The resulting system of equations is solved using a GMRES Krylov solver preconditioned with a Jacobi algorithm, similar to the solution strategy for the flow. The governing equations for the mesh deformation problem can be written symbolically as:

$$\mathbf{G}(\mathbf{x},\mathbf{D}) = \mathbf{0} \tag{8}$$

where $\mathbf{x}$ denotes the interior mesh coordinates and $\mathbf{D}$ denotes shape parameters that define the surface geometry.

II.C. Geometry parameterization

Modifications to the baseline airfoil geometry are achieved by displacing the nodes of the airfoil using the Class function - Shape function Transformation geometry parameterization technique.[21] This parameterization technique gives an equation for the upper and lower surface of the airfoil as

$$y_{upper}(x) = C(x)Su(x) + x\Delta y_{upper} \tag{9}$$
$$y_{lower}(x) = C(x)Sl(x) + x\Delta y_{lower}$$

for a unit chord airfoil. $C(x)$ is the class function, that for an airfoil is

$$C(x) = \sqrt{x}(1-x) \tag{10}$$

and $\Delta y = \Delta y_{upper} + \Delta y_{lower}$ is the airfoil thickness at the airfoil trailing edge, which in this work is set to zero. $S(x)$ is the shape function defined as

$$Su(x) = \sum_{i=1}^{N} Au_i S_i(x)$$
$$Sl(x) = \sum_{i=1}^{N} Al_i S_i(x) \tag{11}$$

In equation (11) N is the order of the Bernstein polynomial used to describe the airfoil surface and the terms Au_i and Al_i are the $i-th$ design parameter on the upper and lower surface respectively used to scale the $i-th$ $S_i(x)$ term in the Bernestein polynomial defined in equation (12).

$$BPn = \sum_{i=1}^{N} S_i(x)$$
$$S_i(x) = \frac{N!}{i!\,(N-i)!}\, x^i\,(1-x)^{N-1} \tag{12}$$

Bernstein polynomials of order eight have been implemented in this work, for a total of 16 design variables. The design variables Au_i and Al_i for the baseline airfoil have been determined with a non-linear least square fit to the NACA-0012 airfoil coordinate.

American Institute of Aeronautics and Astronautics
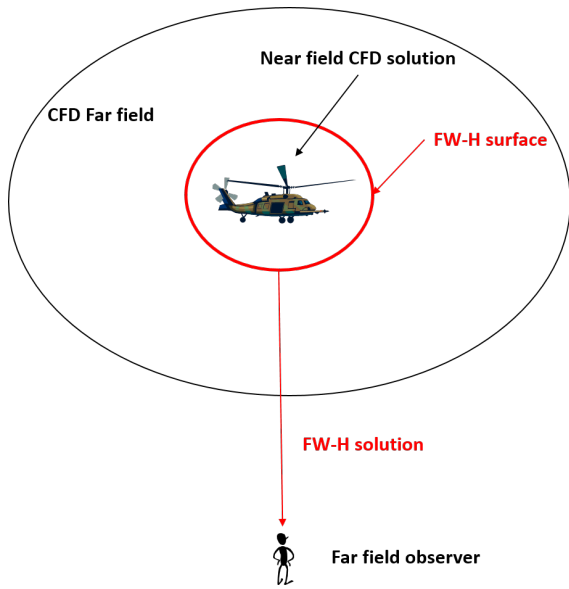
(a) Schematics of the hybrid approach for the aeroacoustic computation
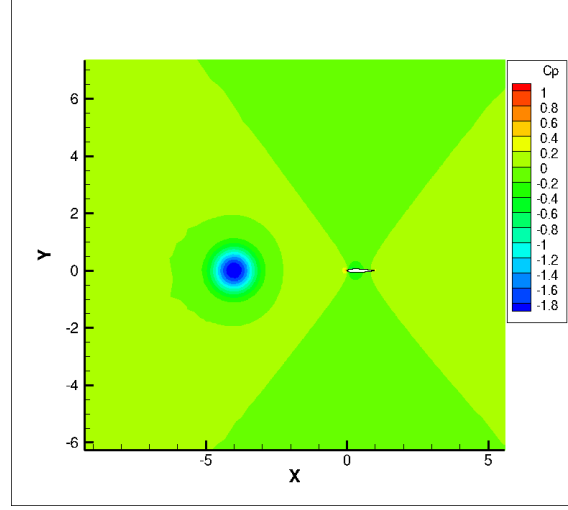
(b) Vortex initialization after the steady state solution has been reached.

Figure 1: Schematics of the hybrid acoustic approach (a) and initialization of the isentropic vortex in the CFD domain (b)

III. Blade vortex interaction noise

The focus of this work is to develop an adjoint-based framework to minimize blade-vortex interaction noise using a hybrid acoustic approach where the near-field Euler CFD solver described in section II provides the input to the FW-H acoustic module as shown schematically in Figure 1(a). The test problem chosen here to validate the newly developed methodology is the interaction of an isentropic vortex[22] with a NACA-0012 airfoil.

The perturbation to the flow generated by the isentropic vortex is described by

$$\delta u = -\frac{\alpha}{2\pi}\left(y - y_0\right)\exp\phi\left(1 - r^2\right)$$
$$\delta v = \frac{\alpha}{2\pi}\left(x - x_0\right)\exp\phi\left(1 - r^2\right)$$
$$\delta T = \frac{\alpha^2\left(\gamma - 1\right)}{16\phi\gamma\pi^2}\exp\phi\left(1 - r^2\right)$$

(13)

where ϕ is a parameter determining the gradient of the solution and α determines the strength of the vortex, $r = \sqrt{\left(x - x_0\right)^2 + \left(y - y_0\right)^2}$ is the distance from the vortex center and $\gamma = 1.4$ is the ratio of specific heats. The vortex center coordinates are x_0 and y_0 and for the case of the head - on airfoil vortex interaction simulated in this work $x_0 = -4.0$ and $y_0 = 0$. The freestream Mach number is $M = 0.6$ and the angle of attack is zero. The flow around the airfoil is first converged to its steady state solution. Once the steady state solution is reached the vortex is initialized in the domain upstream of the airfoil, as shown in Figure 1(b), perturbing the steady state solution using equation (13) and the unsteady computation begins. The vortex is freely convected downstream and it interacts with the airfoil resulting in a complex unsteady flow: 256 timesteps of uniform size $dt = 0.4$ non-dimensionalized with the freestream speed of sound have been used in all the unsteady simulations presented here. Every timestep is converged to machine precision as shown in Figure 2. The flowfield variables from each timestep at the FW-H permeable surface location are then used as input to the acoustic propagation module described in section V. The CFD mesh consists of approximately 60,000 triangular elements clustered mainly around the airfoil. The FW-H surface is a collection of edges from the unstructured mesh and a gradient reconstruction procedure is used to interpolate the solution from the cell center to the edge midpoint used in the FW-H quadrature formula. The FW-H integration can now be performed to predict the acoustic pressure time history and the sound pressure level (SPL) at the observer location.
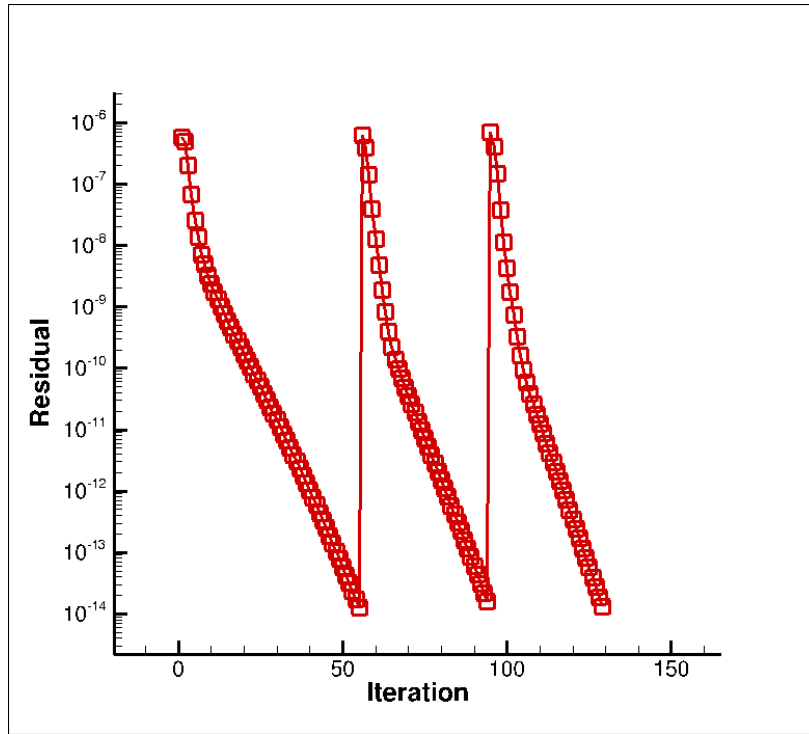
American Institute of Aeronautics and Astronautics

Figure 2: Residual convergence for the first three timestep of the unsteady CFD solution

IV.   Aerodynamic sensitivity analysis formulation for airfoil vortex interaction

The discrete adjoint formulation for the blade vortex interaction described above is presented here for a time-integrated objective function for the BDF1 time discretization scheme for simplicity. The derivation presented here closely follows Mani and Mavriplis.[12]

The objective function L at the end of the time integration process can be expressed as

$$L^n = L^n \left(\mathbf{U^n}(\mathbf{D}), \mathbf{x}(\mathbf{D}) \right) \tag{14}$$

where the superscript n indicates the $n-th$ timestep, $\mathbf{D}$ is the vector of design variables and $\mathbf{x}(\mathbf{D})$ is the vector of mesh nodes displacements that depends on the design variables, but not on time.

The forward linearization of equation (14) can be written as:

$$\frac{dL^n}{dD} = \frac{\partial L^n}{\partial \mathbf{U}^n} \frac{\partial \mathbf{U}^n}{\partial \mathbf{D}} + \frac{\partial L^n}{\partial \mathbf{x}} \frac{\partial \mathbf{x}}{\partial \mathbf{D}} \tag{15}$$

The flow residual at each timestep for a BDF1 time discretization scheme is given as

$$\mathbf{R}^n = \mathbf{R}^n \left(\mathbf{U}^n(\mathbf{D}), \mathbf{U}^{n-1}(\mathbf{D}), \mathbf{x}(\mathbf{D}) \right) = \frac{\mathbf{V} \left(\mathbf{U}^n - \mathbf{U}^{n-1} \right)}{\Delta t} + \mathbf{S}^n(\mathbf{U}^n, \mathbf{n}) \tag{16}$$

where $\mathbf{V}$ is the volume of the control volume, i. e. the area of the cell, and $\mathbf{S}^n(\mathbf{U}^n, \mathbf{n})$ is the spatial residual evaluated at timestep n.

Differentiating equation (16) with respect to a design variable, an expression for $\frac{\partial \mathbf{U}^n}{\partial D}$ to be used in equation (15) is obtained as

$$\frac{\partial \mathbf{U}^n}{\partial D} = - \left[\frac{\partial \mathbf{R}^n}{\partial \mathbf{U}^n} \right]^{-1} \left(\frac{\partial \mathbf{R}^n}{\partial \mathbf{U}^{n-1}} \frac{\partial \mathbf{U}^{n-1}}{\partial D} + \frac{\partial \mathbf{R}^n}{\partial \mathbf{x}} \frac{\partial \mathbf{x}}{\partial D} \right) \tag{17}$$

American Institute of Aeronautics and Astronautics

where $\left[\frac{\partial \mathbf{R}^n}{\partial \mathbf{U}^n}\right]$ is the Jacobian of equation (16) that is inverted using the same GMRES - Krylov algorithm used in the analysis problem. The term $\frac{\partial \mathbf{x}}{\partial D}$ is obtained from

$$[\mathbf{K}] \frac{\partial \mathbf{x}}{\partial D} = \frac{\partial \mathbf{x}_{surf}}{\partial D} \tag{18}$$

where $[\mathbf{K}]$ is the stiffeness matrix of the mesh deformation problem as described in section II.B and $\frac{\partial \mathbf{x}_{surf}}{\partial D}$ is the forward sensitivity of the boundary nodes with respect to the design variables. The system is solved with the GMRES-Krylov algorithm described in section II.B. Once the term $\frac{\partial \mathbf{U}^n}{\partial D}$ has been computed as per equation (17) the objective function sensitivity at the final timestep can be evaluated with the matrix vector products described in equation (15). Equation (17) represents a forward integration in time where the initial condition $\frac{\partial \mathbf{U}^0}{\partial D}$ is given by the linearization of the vortex equations with respect to the design variables.

Transposition of equations (15) gives the reverse linearization of the objective function in equation (14)

$$\frac{dL^n{}^T}{d\mathbf{D}} = \frac{\partial \mathbf{U}^n{}^T}{\partial \mathbf{D}} \frac{\partial L^n{}^T}{\partial \mathbf{U}^n} + \frac{\partial \mathbf{x}}{\partial \mathbf{D}}^T \frac{\partial L^n{}^T}{\partial \mathbf{x}} \tag{19}$$

The term $\frac{\partial \mathbf{U}^n{}^T}{\partial \mathbf{D}}$ is obtained by transposing equation (17) as

$$\frac{\partial \mathbf{U}^n{}^T}{\partial D} = - \left(\frac{\partial \mathbf{R}^n}{\partial \mathbf{U}^{n-1}} \frac{\partial \mathbf{U}^{n-1}}{\partial D} + \frac{\partial \mathbf{R}^n}{\partial \mathbf{x}} \frac{\partial \mathbf{x}}{\partial D} \right)^T \left[\frac{\partial \mathbf{R}^n}{\partial \mathbf{U}^n} \right]^{-T} \tag{20}$$

Substituting equation (20) into equation (19) yields

$$\frac{dL^n{}^T}{d\mathbf{D}} = - \left(\frac{\partial \mathbf{U}^{n-1}{}^T}{\partial D} \frac{\partial \mathbf{R}^n{}^T}{\partial \mathbf{U}^{n-1}} + \frac{\partial \mathbf{x}}{\partial D}^T \frac{\partial \mathbf{R}^n{}^T}{\partial \mathbf{x}} \right) \left[\frac{\partial \mathbf{R}^n}{\partial \mathbf{U}^n} \right]^{-T} \frac{\partial L^n{}^T}{\partial \mathbf{U}^n} + \frac{\partial \mathbf{x}}{\partial \mathbf{D}}^T \frac{\partial L^n{}^T}{\partial \mathbf{x}} \tag{21}$$

and the flow adjoint variable at time level n is now defined as

$$\Lambda_u^n = \left[\frac{\partial \mathbf{R}^n}{\partial \mathbf{U}^n} \right]^{-T} \frac{\partial L^n{}^T}{\partial \mathbf{U}^n} \tag{22}$$

Rearranging equation (23) and using the flow adjoint variable in equation (22) as

$$\frac{dL^n{}^T}{d\mathbf{D}} = - \left(\frac{\partial \mathbf{U}^{n-1}{}^T}{\partial D} \frac{\partial \mathbf{R}^n{}^T}{\partial \mathbf{U}^{n-1}} + \frac{\partial \mathbf{x}}{\partial D}^T \frac{\partial \mathbf{R}^n{}^T}{\partial \mathbf{x}} \right) \Lambda_u^n + \frac{\partial \mathbf{x}}{\partial \mathbf{D}}^T \frac{\partial L^n{}^T}{\partial \mathbf{x}} \tag{23}$$

the mesh adjoint variable at time level n can now be defined as

$$\Lambda_x^n = [\mathbf{K}]^{-T} \left[\frac{\partial L^n{}^T}{\partial \mathbf{x}^n} - \frac{\partial \mathbf{R}^n{}^T}{\partial \mathbf{x}} \Lambda_u^n \right] \tag{24}$$

where $[\mathbf{K}]^{-T}$ is the inverse of the transpose of the stiffness matrix for the mesh problem. Substituting the mesh adjoint in equation (23) yields

$$\frac{dL^n{}^T}{d\mathbf{D}} = - \frac{\partial \mathbf{U}^{n-1}{}^T}{\partial D} \frac{\partial \mathbf{R}^n{}^T}{\partial \mathbf{U}^{n-1}} \Lambda_u^n + \frac{\partial \mathbf{x}_{surf}}{\partial D}^T [\mathbf{K}]^{-T} \left[\frac{\partial L^n{}^T}{\partial \mathbf{x}} - \frac{\partial \mathbf{R}^n{}^T}{\partial \mathbf{x}} \Lambda_u^n \right] \tag{25}$$

and the term $\frac{\partial \mathbf{x}_{surf}}{\partial D}^T$ is the known sensitivity of the boundary nodes with respect to the design variables. It is clear in equation (25) that the sensitivity $\frac{dL^n{}^T}{d\mathbf{D}}$ depends now only on values at previous time steps, hence leading to a backward integration in time and at a given time level $k = n$ the flow and mesh adjoint can be written as

$$\Lambda_u^k = \left[\frac{\partial \mathbf{R}^k}{\partial \mathbf{U}^k} \right]^{-T} \left[\frac{\partial L^k{}^T}{\partial \mathbf{U}^k} - \frac{\partial \mathbf{R}^{k+1}{}^T}{\partial \mathbf{U}^k} \Lambda_u^{k+1} \right] \tag{26}$$

American Institute of Aeronautics and Astronautics

and

$$\Lambda_x^k = [K]^{-T} \left[\frac{\partial L^{k}}{\partial \mathbf{x}^k}^T - \frac{\partial \mathbf{R}^{k+1}}{\partial \mathbf{x}}^T \Lambda_w^{k+1} - \frac{\partial \mathbf{R}^{k}}{\partial \mathbf{x}}^T \Lambda_w^k + \Lambda_x^{k+1} \right] \tag{27}$$

respectively. The final (initial) term $\frac{\partial \mathbf{U}^0}{\partial \mathbf{D}}^T$ is taken from the linearization of the vortex equations with respect to the design parameter in reverse mode. Hence the backward time integration requires the solution of one flow and one mesh adjoint problem at every timestep. The inversion of the flow Jacobian $\left[\frac{\partial \mathbf{R}^n}{\partial \mathbf{U}^n} \right]^T$ is achieved with a GMRES - Krylov algorithm preconditioned with a coloured Gauss - Seidel iteration scheme, while the mesh adjoint problem is solved with a Jacobi preconditioned GMRES - Krylov algorithm. The linear systems in equations (26) and (27) are both converged to machine precision at every timestep as shown in Figure 3
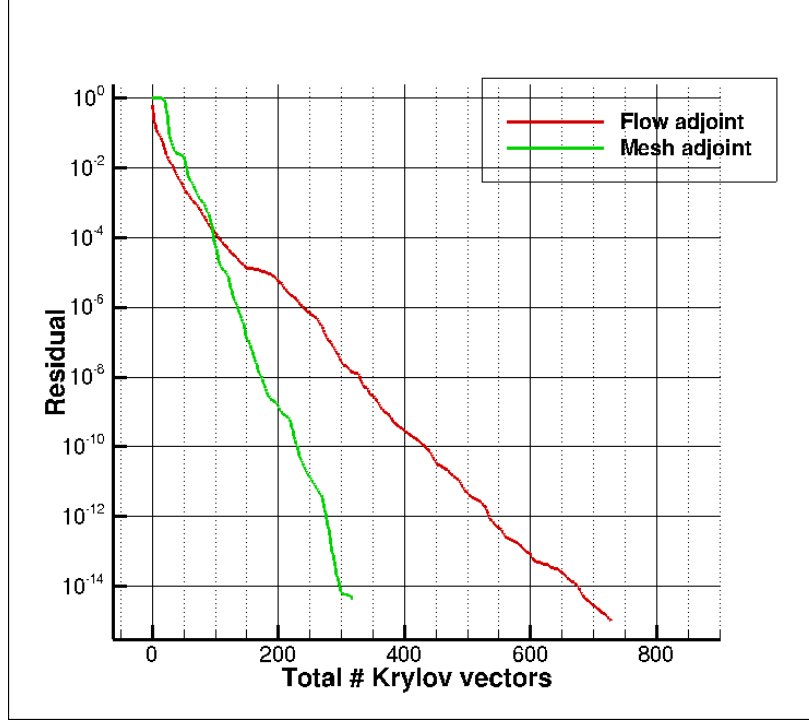

Figure 3: Residual convergence for the flow and the mesh adjoint problems for a generic timestep

In the case of a time-integrated objective function, equation (14) is modified as

$$L^g = L^g \left(L^1, L^2 \cdots, L^n \right) \tag{28}$$

and its forward linearization is

$$\frac{dL^g}{d\mathbf{D}} = \sum_n \left[\frac{\partial L^g}{\partial L^n} \frac{\partial L^n}{\partial \mathbf{U}^n} \frac{\partial \mathbf{U}^n}{\partial \mathbf{D}} + \frac{\partial L^g}{\partial L^n} \frac{\partial L^n}{\partial \mathbf{x}} \frac{\partial \mathbf{x}}{\partial \mathbf{D}} \right] \tag{29}$$

with $\frac{\partial \mathbf{U}^n}{\partial \mathbf{D}}$ and $\frac{\partial \mathbf{x}}{\partial \mathbf{D}}$ that are still computed from equations (17) and (18). The term $\frac{\partial L^g}{\partial L^n}$ is the derivative of the global (time-integrated) objective function L^g with respect to the local (instantaneous) objective function L^n. Once more, transposition of equation (29) gives the adjoint or reverse linearization of equation (28) as

$$\frac{dL^g}{d\mathbf{D}}^T = \sum_n \left[\frac{\partial \mathbf{U}^n}{\partial \mathbf{D}}^T \frac{\partial L^n}{\partial \mathbf{U}^n}^T \frac{\partial L^g}{\partial L^n}^T + \frac{\partial \mathbf{x}}{\partial \mathbf{D}}^T \frac{\partial L^n}{\partial \mathbf{x}}^T \frac{\partial L^g}{\partial L^n}^T \right] \tag{30}$$

Hence, as described by Mani and Mavriplis,[12] the only difference between time-integrated and the non-time-integrated objective function is the pre/post multiplication of the term $\frac{\partial L^n}{\partial \mathbf{U}^n}$ by the global-to-local sensitivity $\frac{\partial L^g}{\partial L^n}$ for the forward/adjoint sensitivity respectively. The two terms $\frac{\partial L^n}{\partial \mathbf{U}^n}$ and $\frac{\partial L^n}{\partial \mathbf{x}}$ drive the backward adjoint time integration: in the case of the acoustic optimization these terms come from the adjoint linearization of the FW-H acoustic module as explained in section VI.

The tangent linearization has been validated against the complex step method.[23] Any function $f(x)$ operating on a real variable x can be used to compute both the function and its derivative $f'(x)$ if the input variable x and all the intermediate variables used in the discrete evaluation of $f(x)$ are redefined as complex variables. In this case for a complex input the function will produce a complex output. A Taylor series of the now complex function $f(x+ih)$, where h is a small step-size and i is the imaginary unit, reads

$$f(x+ih) = f(x) + ihf'(x) + O(h^2) \tag{31}$$

from which the real part is simply the function value at x, while from the imaginary part the function derivative can be easily evaluated as

$$f'(x) = \frac{Im[f(x+ih)]}{h} \tag{32}$$

Despite requiring a step size, as in the case of finite-differencing, the complex step method is insensitive to small step-sizes since no differencing is required. This allows the tangent formulation to be verified to machine precision. Adjoint sensitivities are validated to machine precision with the duality relationship[24] between the tangent and the adjoint formulations. Table 1 shows the comparison between the adjoint linearization and the complex step method for the 7th design variable for the time-integrated aerodynamic objective function defined in equation (46). The error between the complex step method and the flow adjoint demonstrates the accuracy of the adjoint linearization.

Table 1: Complex step validation of the 7th design sensitivity of the flow adjoint.

Adjoint	Complex	Error
-1.7854017702037789E-01	-1.7854017702038E-01	-2.10942374678780E-15

V. Acoustic modeling

Despite the continuous increase in computational resources, numerical simulations that resolve wave propagation from the nearfield to a farfield observer are still infeasible, hence a viable approach to predicting farfield noise level is the use of hybrid methods.

In hybrid methods the finely resolved nearfield flow time history is used as input to an acoustic formulation that predicts the noise radiated to a given observer. The acoustic formulations are often based on Lighthill's acoustic analogy, in particular the Ffowcs Williams-Hawkings (FW-H) approach which is the one used in this work.

The FW-H equation can be expressed in differential form as[19,25]

$$\left(\frac{\partial^2}{\partial t} - c_0^2 \frac{\partial^2}{\partial x_i \partial x_j} \right) (H(f)\rho') = -\frac{\partial F_i \delta(f)}{\partial x_i} + \frac{\partial Q \delta(f)}{\partial t} \tag{33}$$

where

$$Q_i = (\rho_o v_i + \rho(u_i - v_i)) \frac{\partial f}{\partial x_i} \tag{34}$$

and

$$F_i = (p\delta_{ij} + \rho u_i(u_j - v_j)) \frac{\partial f}{\partial x_i} \tag{35}$$

and the Lighthill's stress tensor, the quadrupole term, has been omitted since it is not used in this work. Equation (34) gives rise to an unsteady monopole-type contribution that can be associated with mass addition, while the dipole term, equation (35), involves an unsteady force. The function $f(x_i) = 0$ defines the surface of integration outside of which the solution is sought. Total density and pressure are ρ and p respectively, the fluid velocities are u_i, while v_i are the surface velocities and c_o is the freestream speed of sound. The prime denotes perturbation relative to the freestream which itself is denoted with the subscript o. x_i and t are Cartesian coordinates and time respectively. $H(f)$ is the Heaviside function while $\delta(f)$ is the Dirac function. If the indices i and j run only over 1 and 2 the equation can be considered two dimensional.

American Institute of Aeronautics and Astronautics

Lockard[19] derives a two-dimensional FW-H equation designed to avoid the "tail effect" associated with the time integration of two-dimensional CFD data using a transformation to the frequency domain.
The solution to the two-dimensional differential FW-H equation in the frequency domain reads:

$$H(f)c_0^2\rho' = H(f)p' = -\oint_{f=0} F_i(\xi,\omega)\frac{\partial G(\mathbf{y},\xi)}{\partial \xi_i}dl - \oint_{f=0} Q(\xi,\omega)G(\mathbf{y},\xi)\mathbf{dl} \tag{36}$$

where $\mathbf{y}$ is the observer location, $\xi = (\xi,\eta)$ are the two dimensional source coordinates on the integration surface $f = 0$ under the assumption of uniform rectilinear motion, ω is the frequency, $Q(\xi,\omega)$ and $F_i(\xi,\omega)$ are the monopole and dipole terms at the source locations in the frequency domain and dl is the infinitesimal length along the surface $f = 0$. The function

$$G(\mathbf{y},\xi) = \frac{i}{4\beta}\quad e^{\frac{Mk\bar{x}}{\beta^2}}H_0^2\left(\frac{k}{\beta^2}\sqrt{\bar{x}^2+\beta^2\bar{y}^2}\right) \tag{37}$$

is the free space Green's function, where H_0^2 is the Hankel function of second kind of order zero, and

$$\bar{x} = (x-\xi)\cos\theta + (y-\eta)\sin\theta$$
$$\bar{y} = -(x-\xi)\sin\theta + (y-\eta)\cos\theta$$

where x and y are the observer coordinates, $\tan\theta = V/U$ with V and U being the freestream Cartesian velocities of the flow, $M = \sqrt{U^2+V^2}/c_o$ is the Mach number and $\beta = \sqrt{1-M^2}$ is the Prandtl-Glauert factor.
Numerical computation of the integral in equation (36) is performed in this work with a one point Gaussian quadrature after having assembled the monopole and dipole terms from the time-accurate CFD data and having filtered and transformed their signals in the frequency domain with an FFT transformation. The current implementation has been validated against two analytical test cases, a monopole in uniform flow and the scattering of sound by an edge.[19,25] The complex potential for the monopole in uniform flow is given by Lockard[19] as

$$\phi(\mathbf{x},t) = Ae^{i\omega t}G(\mathbf{y},\xi) \tag{38}$$

where A is the amplitude, ω is the frequency, t is time and $G(\mathbf{y},\xi)$ is the Green's function defined in equation (37). Equation (38) gives the value of the potential at any point in space and time and the variables needed for the FW-H integration are obtained by taking the real part of $p' = -\rho_o(\frac{\partial\phi}{\partial t}+U_i\frac{\partial\phi}{\partial x_i})$, $u'_i = \frac{\partial\phi}{\partial x_i}$ and using the isentropic condition $\rho' = p'/c_o^2$ with c_o being the freestream speed of sound. The FW-H is then validated by first evaluating the exact acoustic pressure at the observer location. Then all the variables needed to evaluate the FW-H integral in equation (36) are evaluated at the FW-H surface and the integration is performed. The acoustic prediction is then compared to the exact analytical solution. Results for this test case are shown in Figure 4 showing excellent agreement between the exact solution and the FW-H prediction. The same procedure is followed for the scattering of sound by an edge. A vortex of strength k moves around the edge of a semi infinite plate along the path shown in Figure 5. The vortex reaches its maximum speed when it is closest to the plate, reaching a Mach number $M = 0.001$. The potential for this flow is given by Crighton[25] as:

$$\phi(\mathbf{x},t) = \frac{2\sqrt{2}}{[M^2(r-t)^2+4]^{\frac{1}{4}}}\frac{sin(\frac{\theta}{2})}{r^{\frac{1}{2}}} \tag{39}$$

where $r = \sqrt{x^2+y^2}$ is the radial distance from the origin to a general (x,y) location in the 2D plane, non dimensionalized with the distance b in Figure 5 and θ is the angle measured relative to the positive x-axis. Results for this case are shown in Figure 6 confirming the good prediction of the current FW-H implementation.

V.A.   Sensitivity formulation for the FW-H equation

The functional dependencies for the quantities in equation (36) are as follows
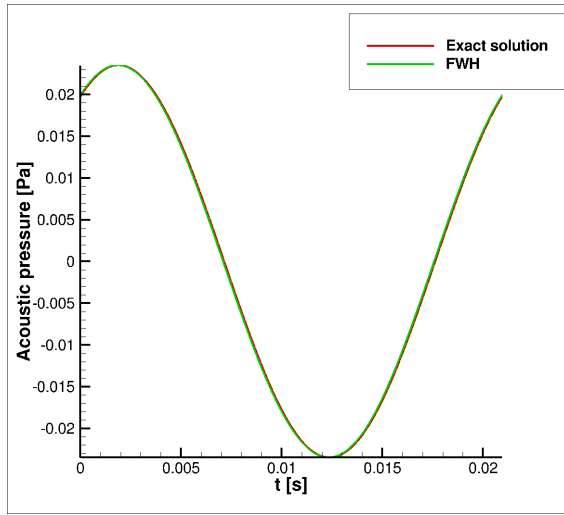
(a) Exact and FWH acoustic pressure solution for an observer at $r = 500m$ for a monopole in uniform flow
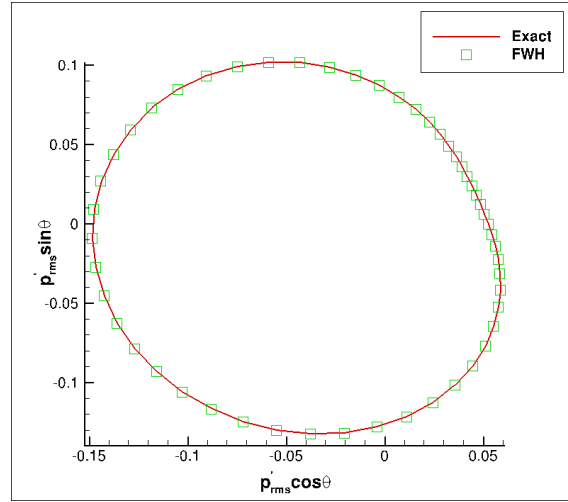
(b) Directivity plot for the monopole in uniform flow[19]

Figure 4: Validation of the acoustic solver for the monopole in uniform flow test case[19]

$$Q = Q(\mathbf{x}_s(\mathbf{D}), \mathbf{U}(\mathbf{D}), \omega) \tag{40}$$
$$F_i = F_i(\mathbf{x}_s(\mathbf{D}), \mathbf{U}(\mathbf{D}), \omega)$$
$$G = G(\mathbf{x}_s(\mathbf{D}), \mathbf{x}_o, \omega)$$
$$\frac{\partial G}{\partial \mathbf{x}_s} = \frac{\partial G}{\partial \mathbf{x}_s}(\mathbf{x}_s(D), \mathbf{x}_o, \omega)$$

where $\mathbf{x_s}(\mathbf{D})$ is the discrete source location on the discrete FW-H integration surface, $\mathbf{x_o}$ is the observer location and ω is the frequency. From equation (40) it is evident that the monopole and dipole terms depend on the design parameters $\mathbf{D}$ through both the FW-H surface geometry and the input CFD solution. The acoustic pressure at the observer can then be expressed as

$$p(\mathbf{D}, \omega) = \mathbf{FWH}(\mathbf{U}(\mathbf{D}, \omega), \mathbf{x}(\mathbf{D}), \omega) \tag{41}$$

where $FWH(\mathbf{U}(\mathbf{D}, \omega), \mathbf{x}(\mathbf{D}), \omega)$ represents all the discrete operations necessary to evaluate equation (36) numerically, as described above. Differentiation of equation (41) with respect to the design variables yields the pressure sensitivity at the observer as

$$\frac{dp(\mathbf{D}, \omega)}{dD} = \sum_n \frac{\partial FWH}{\partial \mathbf{U^n_{FWH}}} \frac{\partial \mathbf{U^n_{FWH}}}{\partial D} + \frac{\partial FWH}{\partial x_{FWH}} \frac{\partial x_{FWH}}{\partial D} \tag{42}$$

where it is intended that $\frac{\partial \mathbf{U^n_{FWH}}}{\partial D}$ is the tangent CFD solution at the $n-th$ timestep at the surface location and $\frac{\partial x_{FWH}}{\partial D}$ is the CFD mesh sensitivity at the FWH integration surface, while the matrices $\frac{\partial FWH}{\partial \mathbf{U}_{FWH}}$ and $\frac{\partial FWH}{\partial \mathbf{x}_{FWH}}$ have been obtained by linearization of each component in the acoustic solver. The term $\frac{\partial x_{FWH}}{\partial D}$ has been included here for the sake of generality as it could be set to zero by constraining the CFD mesh deformation at the FW-H integration surface, although this approach has not been followed in this work and it could not be followed in the case of a solid wall FW-H integration surface.

The time-integrated acoustic objective function used in this work is the sound pressure level (SPL) at an observer location, defined as in equation (43)

$$L_{FWH} = SPL(p(D)) = 20\log_{10}\left(\frac{p_{RMS}}{p_0}\right) \tag{43}$$
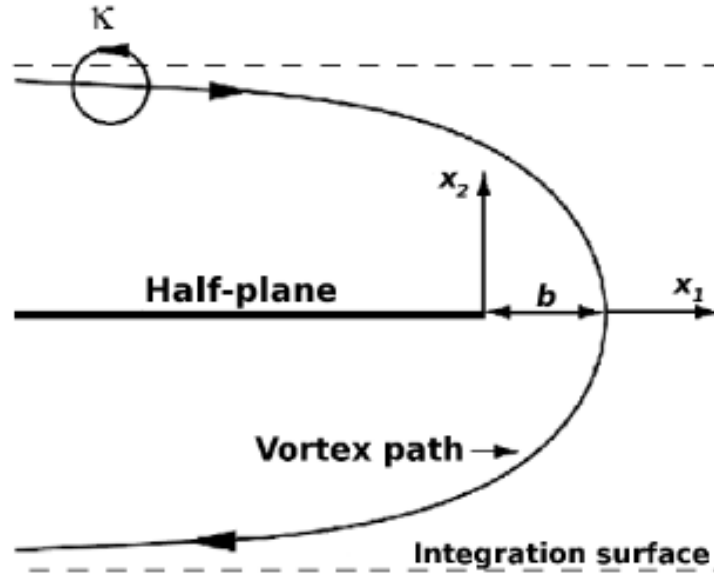
Figure 5: Schematic of the scattering by an edge from Rumpfkeil[16]

where p_{RMS} is the root mean square of the acoustic pressure at the observer and $p_0 = 20\mu Pa$ is a reference pressure. Thus the final form of the objective sensitivity reads:

$$\frac{dL_{FWH}}{dD} = \sum_n \frac{\partial L_{FWH}^n}{\partial U_{FWH}^n} \frac{\partial U_{FWH}^n}{\partial D} + \frac{\partial L_{FWH}}{\partial x_{FWH}} \frac{\partial x_{FWH}}{\partial D} = \frac{\partial SPL}{\partial p} \frac{\partial p}{\partial D} = \frac{\partial SPL}{\partial p} \left[\sum_n \frac{\partial FWH}{\partial \mathbf{U_{FWH}^n}} \frac{\partial \mathbf{U_{FWH}^n}}{\partial D} + \frac{\partial FWH}{\partial x_{FWH}} \frac{\partial x_{FWH}}{\partial D} \right] \quad (44)$$

VI.   Coupling of the flow and acoustic solvers for analysis, tangent and adjoint problems

The flow and the acoustic analysis codes are loosely coupled and the FW-H acoustic propagation model can be considered a post-processing step of the unsteady CFD simulation. The non-conserved variables of the CFD solution must be extracted at the source locations on the FW-H integration surface for the complete time history. Since the CFD solver is a cell-centered solver and the FW-H surface is a concatenation of edges from the unstructured CFD mesh an unlimited least-square gradient reconstruction procedure is employed to guarantee second-order accuracy while extracting the CFD data at the acoustic surface location. The edges of the FW-H surface are chosen using a wall distance criterion four chords away from the airfoil and the approximate location of the surface is shown in Figure 7. The extracted CFD solution time history is then used as input to the FW-H acoustic solver and the acoustic objective function can be computed. The very same procedure is followed to couple the tangent flow and the tangent acoustic codes. The complete time history of the flow sensitivity must be reconstructed at the FW-H integration surface, then both the flow and the mesh sensitivities at the integration surface can be passed as input to the tangent FW-H solver and finally the sensitivity of the time-integrated objective function, the sound pressure level at the observer, can be computed.

Thus, the sensitivity in equation (44) can be computed once the vectors $\frac{\partial \mathbf{U}^n}{\partial D}$ and $\frac{\partial \mathbf{x}}{\partial D}$ are known at the FW-H surface from the flow tangent problem. Hence the tangent FW-H solver is a post-processing step of the flow tangent problem. The tangent FW-H solver has been validated with a finite difference approach as the complex-step method[23] is not applicable in this case since the acoustic analysis equation itself includes complex variables via the Green's function, equation (37). A comparison between the propagated and the computed observer acoustic pressure sensitivity is shown in Figure 8 for two different observer locations. In Figure 8(a) the observer is placed underneath the airfoil at the center of a CFD cell approximately 0.4 chords away from the FW-H integration surface while in Figure 8(b) the observer is approximately 1.5 chords away and for both cases the acoustic pressure sensitivity computed by the tangent flow solver can be compared to that propagated by the tangent FW-H solver. Figure 8 shows good agreement between the two codes. Note that the tangent CFD solution consistently underestimates all the peaks in the sensitivity time history, a consequence of the numerical dissipation associated with the current space discretization. Furthermore, this behaviour deteriorates as the observer is placed further away from the FW-H integration surface.

American Institute of Aeronautics and Astronautics
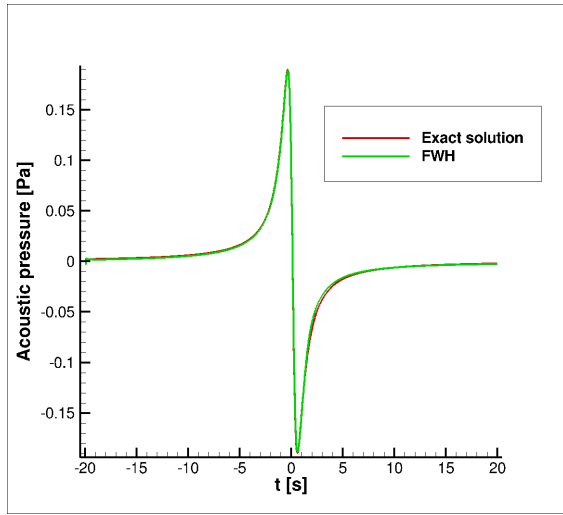
(a) Exact and FWH acoutic pressure solution for an observer at $r =$ 50m for a vortex passing over an edge
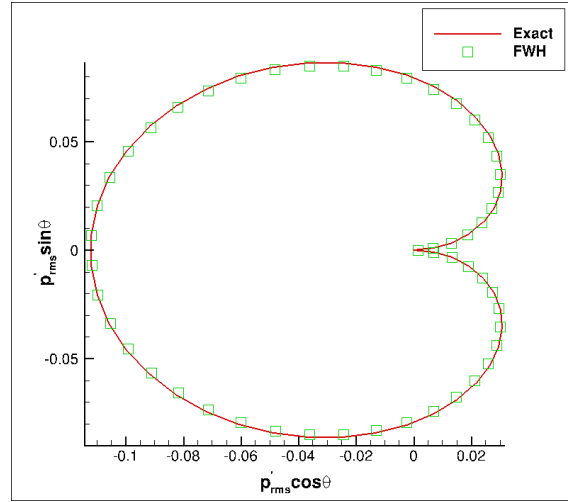
(b) Directivity plot for the vortex over edge flow[25]

Figure 6: Validation of the acoustic solver for the scattering of sound by an edge[25]

Transposing equation (44) yields the adjoint linearization of the acoustics objective fuction as

$$\frac{dL_{FWH}}{dD}^T = \sum_n \frac{\partial U^n}{\partial D}^T \frac{\partial L^n_{FWH}}{\partial U^n}^T + \frac{\partial x}{\partial D}^T \frac{\partial L_{FWH}}{\partial x}^T \tag{45}$$

The terms $\frac{\partial L^n_{FWH}}{\partial U^n_{FWH}}^T$ and $\frac{\partial L_{FWH}}{\partial x}^T$ are known once the products $\frac{\partial FWH}{\partial \mathbf{U}_{FWH}}^T \frac{\partial SPL}{\partial p}^T$ and $\frac{\partial FWH}{\partial \mathbf{x}_{FWH}}^T \frac{\partial SPL}{\partial p}^T$ have been evaluated. These two matrix - vector products are the adjoint linearization of the discrete FW-H equation and are obtained by transposition of the corresponding matrices in the forward linearization. Equation (45) is now in the form of equation (30) and the backward time integration described in section IV can start with $\frac{\partial L^n}{\partial U^n}^T = \frac{\partial L^n_{FWH}}{\partial U^n_{FWH}}^T = \frac{\partial FWH}{\partial \mathbf{U}_{FWH}}^T \frac{\partial SPL}{\partial p}^T$ and $\frac{\partial L}{\partial x}^T = \frac{\partial L_{FWH}}{\partial x}^T = \frac{\partial FWH}{\partial \mathbf{x}_{FWH}}^T \frac{\partial SPL}{\partial p}^T$. Hence the adjoint of the acoustic module can be considered a preprocessing step to the flow adjoint solver described in IV. Once these two terms are known the flow adjoint solver can start as described in section IV. The adjoint solver has been validated by the duality-relation[24] to the tangent solver to machine precision. Table 2 shows the finite difference validation of the 7th adjoint design sensitivity. A second order accurate centered finite difference scheme with a step $\delta D = 1e - 4$ has been used.

Table 2: Finite difference validation of the 7th design sensitivity.

Adjoint	FD	Error
-3.1819940460451508E-03	-3.17975314778490E-03	2.24089826024758E-06

VII.   Optimization results

Loosely speaking the goal of the following optimizations is to reduce the noise signature at an observer location without suffering significant aerodynamic penalties. In a three dimensional framework the optimization goal would be to minimize the observer noise under the condition that the helicopter rotor is trimmed. In the present two dimensional framework the trim condition is replaced by requiring that the optimized airfoil time-integrated lift is constrained to that of the baseline NACA-0012 airfoil, hence the aerodynamic constraint for the present two dimensional optimization
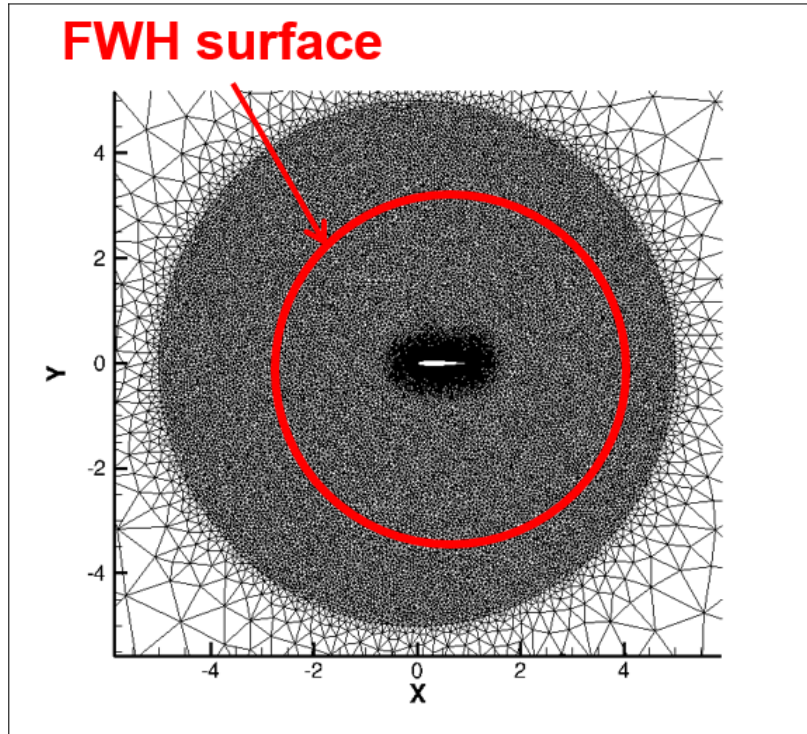
Figure 7: CFD mesh and approximate location of the FW-H integration surface

is expressed as shown in equation (46)

$$L_{AERO} = \frac{\sum_{n=1}^{Ntsteps} \left(C_L^n - C_{L_{baseline}}^n \right)^2}{N_{tsteps}} \tag{46}$$

while the sound pressure level has been chosen as a measurement of the noise signature at the observer and the acoustic objective function is defined as in equation (47)

$$L_{FWH} = \frac{SPL_{@x=0.5,y=-50}}{SPL_{baseline}} \tag{47}$$

where $SPL_{baseline} = 87.1 dB$ is the sound pressure level of the baseline NACA - 0012 airfoil at the same observer location. Two different optimization algorithms have been used in this work: the L-BFGS-B quasi-Newton method from Zhu[26] and the sequential quadratic programming (SQP) algorithm implemented in SciPy.[27] The two algorithms differ in that the L-BFGS-B is an unconstrained optimization algorithm while the SQP algorithm can handle linear and nonlinear, equality and inequality constraints. This difference reflects on the way the optimization problem is defined since in the L-BFGS-B optimization the aerodynamic constraint must be enforced as a penalty term in the objective function and only one adjoint solution is required, while the strong enforcement of the aerodynamic constraint in the SQP optimization requires two different adjoint solutions, one for the acoustic objective function and one for the aerodynamic constraint.

VII.A. L-BFGS-B optimization

The objective function for the L-BFGS-B optimization algorithm is taken as

$$L^g = \omega L_{FWH} + (1 - \omega) L_{AERO} \tag{48}$$

where the acoustic and the aerodynamic objective function have been defined in equation (47) and (46) respectively and ω is a parameter that varies between zero and one and enforces the aerodynamic constraint as a penalty term. For $\omega = 1$ there is no aerodynamic penalty, while the case $\omega = 0$ corresponds to a pure aerodynamic optimization. Figure 9 shows the baseline, the acoustically optimized ($\omega = 1$) and the aerodynamically penalized ($\omega = 0.1$) airfoils.

American Institute of Aeronautics and Astronautics
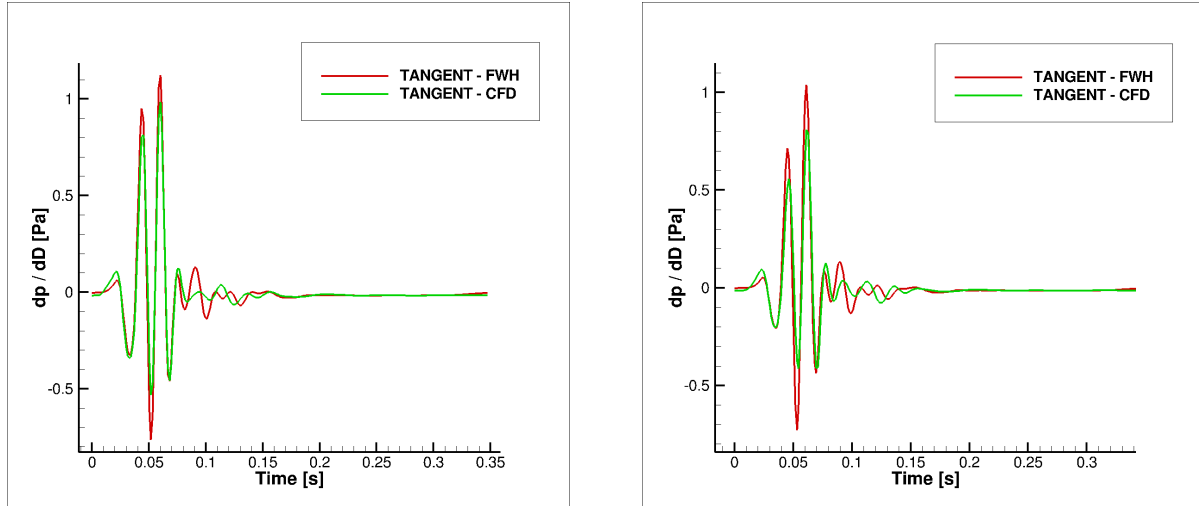
(a) Propagated and computed acoustic pressure sensitivity for an observer 0.4 chords away from the FW-H integration surface

(b) Propagated and computed acoustic pressure sensitivity for an observer 1.5 chords away from the FW-H integration surface

Figure 8: Comparison of FW-H propagated and CFD computed acoustic pressure sensitivity at different observer locations highlighting the detrimental effect that numerical dissipation has on the computed acoustic pressure sensitivity as the observer is moved to the far field.

For the $\omega = 1$ case the optimizer reduces the lower surface thickness and increases the upper surface thickness of the airfoil. The effect of the aerodynamic penalty term is evident in the shape for the $\omega = 0.1$ optimization where an almost symmetric shape is recovered although the chordwise thickness distribution of the optimized airfoil is significantly different from that of the baseline NACA-0012. The lift time histories for the two optimizations and for the baseline airfoil are shown in Figure 10 where it is evident how the aerodynamically penalized optimization tries to recover the baseline lift time history. Convergence of the optimization for the $\omega = 0.1$ case is shown in Figure 11. The objective function reaches a plateau already after 10 iterations while the gradient magnitude is reduced more than one order of magnitude, suggesting that an optimum has in fact been reached. In terms of noise signature the unconstrained optimization ($\omega = 1$) has an SPL $3dB$ lower than the baseline airfoil, while the aerodynamically penalized optimization ($\omega = 0.1$) reduces the baseline SPL of approximately $1dB$, as shown in Table 3.

Table 3: Sound Pressure Level (SPL) values for different weights ω.

	SPL [dB]
Baseline	87.1
$\omega = 0.1$	86.3
$\omega = 1.0$	84.8

VII.B.   Sequential quadratic programming optimization

The optimization problem for the SQP optimization can be formulated as in equation (49)

$$\text{Minimize } L_{FWH}$$
$$\text{Subject to} \tag{49}$$
$$L_{AERO} = 0$$

where now the aerodynamic constraint is strongly enforced and this requires the solution of an extra adjoint problem for the constraint. The SQP optimized airfoil shape is shown in Figure 12 together with the penalized L-BFGS-B and the baseline airfoil. The sound pressure level for SQP optimized airfoil is 86.5dB which is comparable to the penalized

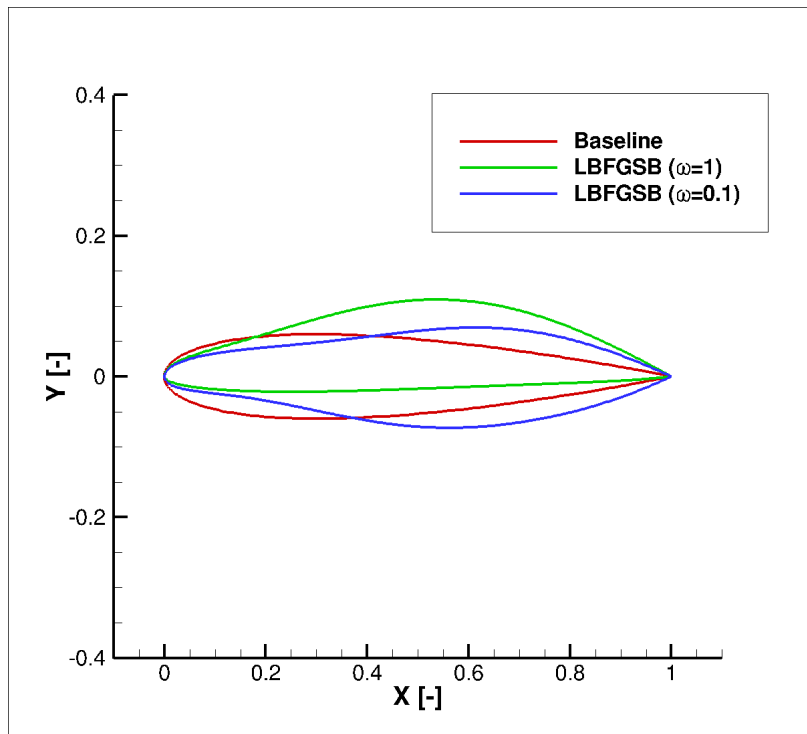American Institute of Aeronautics and Astronautics

Figure 9: Baseline, acoustically optimized ($\omega = 1$) and aeroacoustically optimized ($\omega = 0.1$) airfoils

L-BFGS-B SPL value reported in Table 3. However, despite an almost identical optimized SPL value the two airfoil shapes differ significantly, with the SQP airfoil that considerably departs from the almost symmetric shape of the penalized L-BFGS-B shape. This is a consequence of the direct enforcement of the aerodynamic constraint, as shown in Figure 13 where the lift time histories of the two optimizations are compared to that from the baseline NACA-0012 airfoil. The convergence behaviour of the SQP optimization is shown in Figure 14. The objective function reaches a minimum after approximately 30 iterations compared to the 10 iterations from the L-BFGS-B algorithm, while the gradient magnitude is only slightly reduced. The reason of this convergence behavior is currently being investigated.

## VIII.   Conclusions and future work

We successfully developed an adjoint based formulation for the hybrid approach to the acoustic propagation problem. The new formulation has been applied to the model problem of noise minimization for the interaction of a NACA 0012 airfoil with an isentropic vortex with good results. Two optimization algorithms have been used and the quasi - Newton L-BFGS-B method shows superior performance compared to the SQP optimization, although the convergence behavior of the sequential quadratic programming algorithm is currently being investigated further. In future works the current adjoint framework will be used for spatial and temporal error estimation purposes. The use of higher order temporal integration scheme will also be investigated. Extension of the current methodology to three dimensional problem is currently in progress.

IX.   Acknowledgements

References

[1]Johnson, W., *Rotorcraft aeromechanics*, Cambridge University Press, 2013.

American Institute of Aeronautics and Astronautics
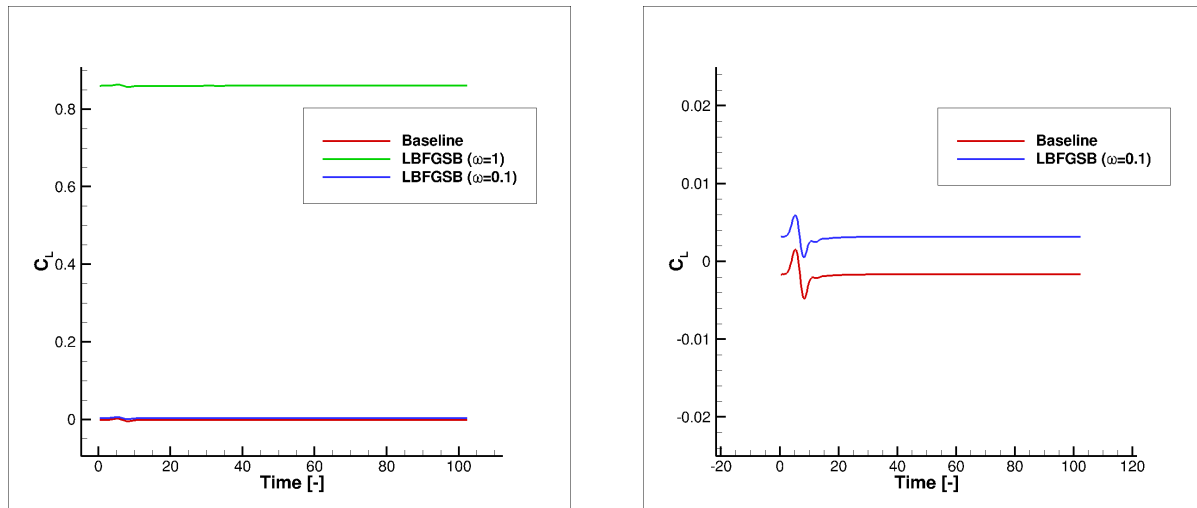
(a) Lift time histories for the baseline, the acoustically optimized ($\omega = 1$) and the aeroacoustically optimized ($\omega = 0.1$) airfoils

(b) Detail of the lift time histories for the baseline and the aeroacoustically optimized ($\omega = 0.1$) airfoils

Figure 10: Lift time histories for the baseline and the optimized airfoil highlithing the importance of the aerodynamic penalty term

[2]Yu, Y. H., "Rotor blade vortex interaction noise," *Progress in Aerospace Sciences*, Vol. 36, 2000, pp. 97–115.

[3]JanakiRam, R. D., Sim, B. W., Kitaplioglu, C., and Straub, F. K., "Blade Vortex Interaction Noise Characteristics of a Full-Scale Active Flap Rotor," 65th Annual Forum of the American Helicopter Society, 2009.

[4]Hicks, R. and Henne, P., "Wing Design by Numerical Optimization," *Journal of Aircraft*, Vol. 15-7, 1978, pp. 407–412.

[5]Jameson, A., "Aerodynamic Shape Optimization using the Adjoint Method," VKI Lecture Series on Aerodynamic Drag Prediction and Reduction, von Karman Institute of Fluid Dynamics, Rhode St Genese, Belgium, 2003.

[6]Jameson, A. and Vassberg, J., "Computational Fluid Dynamics for Aerodynamic Design: Its Current and Future Impact," Proceedings of the 39th Aerospace Sciences Meeting and Exhibit, Reno NV, AIAA Paper 2001–0538, 2001.

[7]Nadarajah, S. and Jameson, A., "A Comparison of the Continuous and Discrete Adjoint Approach to Automatic Aerodynamic Optimization," Proceedings of the 38th Aerospace Sciences Meeting and Exhibit, Reno NV, AIAA Paper 2000–0667, 2000.

[8]Nielsen, E. and Anderson, W., "Recent Improvements in Aerodynamic Design Optimization on Unstructured Meshes," *AIAA Journal*, Vol. 40-6, June 2002, pp. 1155–1163.

[9]Jameson, A., Alonso, J., Reuther, J., Martinelli, L., and Vassberg, J., "Aerodynamic shape optimization techniques based on control theory," AIAA Paper 98–2538, 1998.

[10]Giles, M., Duta, M., and Muller, J., "Adjoint Code Developments Using Exact Discrete Approach," AIAA Paper 2001–2596, 2001.

[11]Nadarajah, S. and Jameson, A., "Optimal Control of Unsteady Flows using A Time Accurate Method," Proceedings of the 9th AIAA/ISSMO Symposium on Multidisciplinary Analysis and Optimization Conference, Atlanta GA, AIAA Paper 2002–5436, 2002.

[12]Mani, K. and Mavriplis, D. J., "Unsteady Discrete Adjoint Formulation for Two-Dimensional Flow Problems with Deforming Meshes," *AIAA Journal*, Vol. 46-6, June 2008, pp. 1351–1364.

[13]Mavriplis, D. J., "Solution of the Unsteady Discrete Adjoint for Three-Dimensional Problems on Dynamically Deforming Unstructured Meshes," Proceedings of the 46th AIAA Aerospace Sciences Meeting, Reno, NV, AIAA Paper 2008–0727, 2008.

[14]Rumpfkeil, M. and Zingg, D., "A General Framework for the Optimal Control of Unsteady Flows with Applications," 45th AIAA Aerospace Sciences Meeting and Exhibit, Reno, NV, January, AIAA Paper 2007–1128, 2007.

[15]Mani, K. and Mavriplis, D. J., "Adjoint based sensitivity formulation for fully coupled unsteady aeroelasticity problems," *AIAA Journal*, Vol. 47, (8), August 2009, pp. 1902–1915.

[16]Rumpfkeil, M., *Airfoil Optimization For Unsteady Flows With Application To High-Lift Noise Reduction*, Ph.D. thesis, University of Toronto, 2008.

[17]Nielsen, E. J., Diskin, B., and Yamaleev, N., "Discrete Adjoint-Based Design Optimization of Unsteady Turbulent Flows on Dynamic Unstructured Grids," *AIAA Journal*, Vol. 48-6, June 2010, pp. 1195–1206.

[18]Mishra, A., Mani, K., Mavriplis, D., and Sitaraman, J., "Helicopter Rotor Design using Adjoint-based Optimization in a Coupled CFD-CSD Framework," 69th Annual Forum of the American Helicopter Society, 2013.

[19]Lockard, D. P., "An efficient Two-Dimensional Implementation of the Ffowcs Williams and Hawkings Equation," *Journal of Sound and Vibration*, Vol. 224-4, 2000, pp. 897–911.

[20]Mavriplis, D. J., "Unstructured-Mesh Discretizations and Solvers for Computational Aerodynamics," *AIAA Journal*, Vol. 46-6, June 2008, pp. 1281–1298.

[21]Kulfan, B. M., "Universal Parametric Geometry Representation Method," *Journal of Aircraft*, Vol. 45-1, 2008, pp. 142–158.

[22]Yee, H. C., Sandham, N. D., and Djomehri, M. J., "Low-Dissipative High-Order Shock-Capturing Methods Using Characteristic-Based Filters," *Journal of Computational Physics*, Vol. 150, 1999, pp. 199–238.
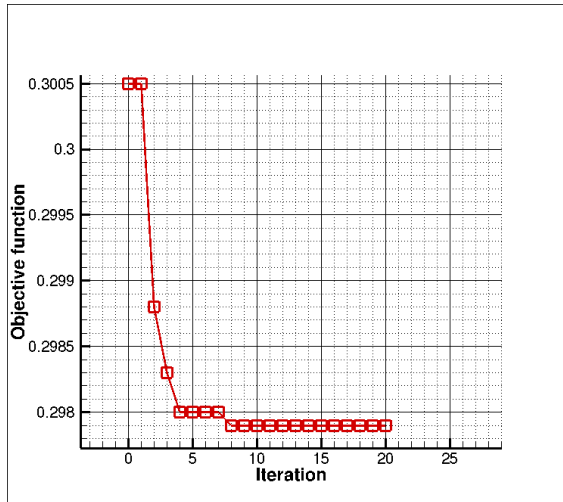
(a) Objective as function of the number of iterations
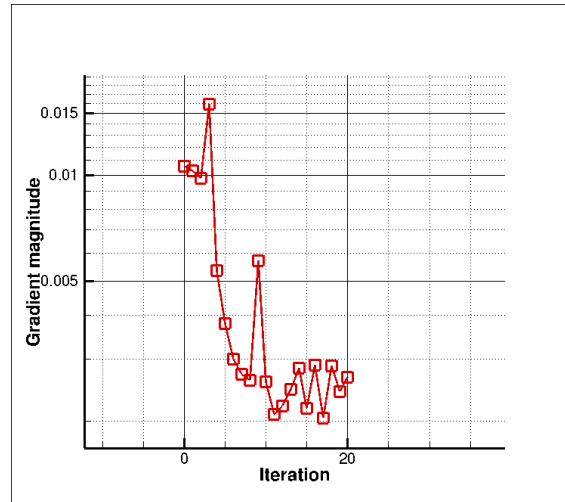
(b) Gradient magnitude as function of the number of iterations

Figure 11: Convergence of the L-BFGS-B $\omega = 0.1$ optimization

[23]Martins, J. R. R. A. S. P. and Alonso, J. J., "The Complex-Step Derivative Approximation," *ACM Transactions on Mathematical Software*, Vol. 29-3, 2003, pp. 245–262.

[24]Mavriplis, D. J., "Discrete Adjoint-Based Approach for Optimization Problems on Three-Dimensional Unstructured Meshes," *AIAA Journal*, Vol. 45-4, April 2007, pp. 741–750.

[25]Crighton, D. G., Dowling, A. P., and Ffowcs Willliams, J. E., *Modern Methods in Analytical Acoustics*, Springer-Verlag, 1992.

[26]Zhu, C., Byrd, R. H., Lu, P., and Nocedal, J., "L-BFGS-B - FORTRAN Subroutines for Large-scale Bound Constrained Optimization," Technical report, Department of Electrical Engineering and Computer Science, December 31 1994.

[27]"http://www.scipy.org/," .

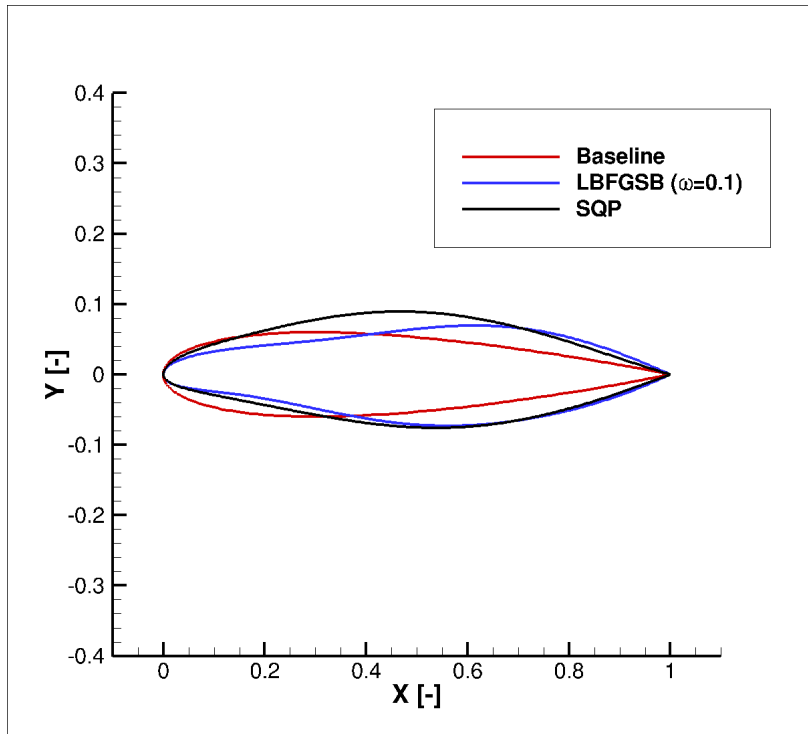American Institute of Aeronautics and Astronautics

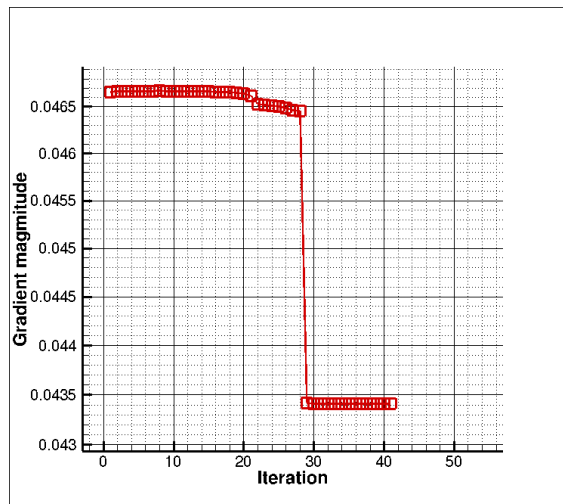Figure 12: Baseline, L-BFGSB-B ($\omega = 0.1$) and SQP optimized airfoils.
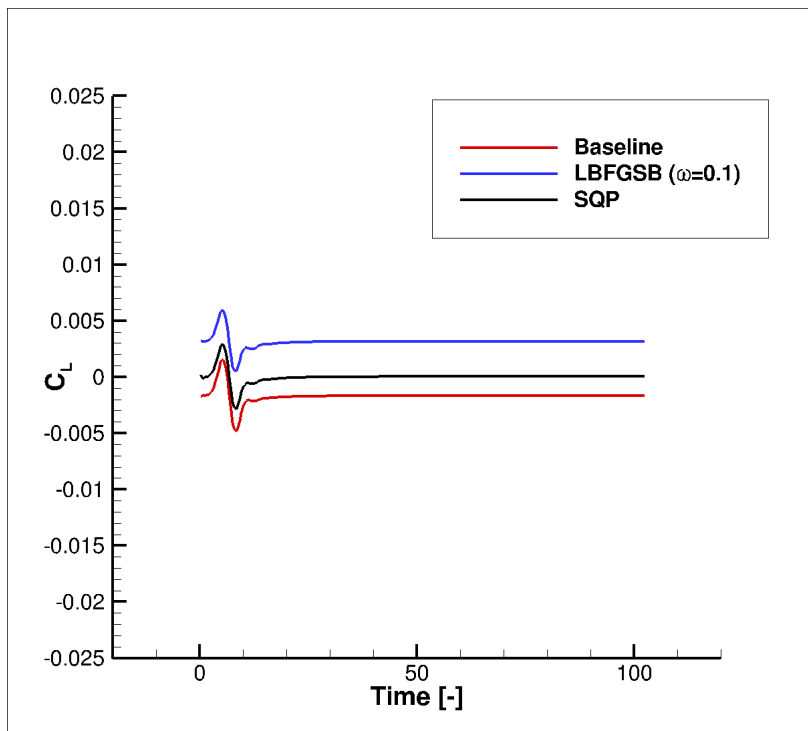
Figure 13: Baseline, L-BFGSB-B ($\omega = 0.1$) and SQP lift time histories.
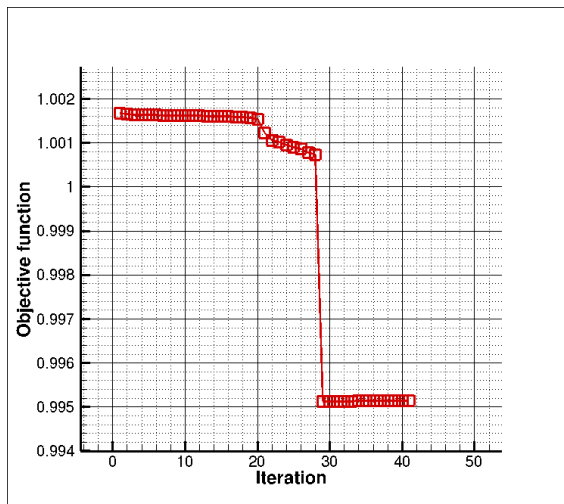
American Institute of Aeronautics and Astronautics

(a) Objective as function of the number of iterations

(b) Gradient magnitude as function of the number of iterations

Figure 14: Convergence of the Sequential Quadratic Programming optimization

American Institute of Aeronautics and Astronautics